673

Simultaneous acquisition of [^{13}C,^{15}N]- and [^{15}N,^{15}N]-separated 4D gradient-enhanced NOESY spectra in proteins

Bennett T. Farmer II* and Luciano Mueller

Macromolecular NMR, Pharmaceutical Research Institute, Bristol-Myers Squibb, P.O. Box 4000, Princeton, NJ 08543-4000, U.S.A.

SUMMARY

The simultaneous acquisition of a 4D gradient-enhanced and sensitivity-enhanced [^{13}C,^{15}N]/[^{15}N,^{15}N]-separated NOESY is presented for the 74-residue [^{13}C,^{15}N]-labeled N-terminal SH3 domain of mGrb2 complexed with a peptide fragment from mSOS-2 in 90% H$_2$O. The method readily accommodates different ^{13}C and ^{15}N spectral widths, but requires that the same number of increments be collected for both ^{13}C and ^{15}N in the simultaneous dimension (F$_2$). For purposes of display and analysis, the two 4D spectra can be deconvolved during the processing stage by the appropriate linear combination of separately stored FIDs. Compared to collecting each of these two 4D data sets separately, the presented method is a factor (2)$^{\frac{1}{2}}$ more efficient in sensitivity per unit acquisition time. The interleaved nature of this method may also lead to improved peak registration between the two 4D spectra.

INTRODUCTION

The [^{13}C,^{15}N]-, [^{15}N,^{15}N]- and [^{13}C,^{13}C]-separated 4D NOESY experiments have become indispensable in the reliable assignment of NOEs in large proteins (Clore et al., 1990; Kay et al., 1990; Zuiderweg et al., 1991). One heteronuclear-edited 4D NOESY experiment typically lasts 5–6 days and therefore constitutes a considerable drain on instrument resources. If two such 4D experiments could be collected in a noncompromising and truly simultaneous manner, a significant reduction in instrument time could be achieved for a given overall signal-to-noise (S/N) level. To this end, the simultaneous acquisition of a ^{13}C/^{15}N-^{1}H HMQC has been previously demonstrated (Farmer II, 1991). This experiment did not compensate for the different magnitudes of ^{1}J$_{CH}$ and ^{1}J$_{NH}$; rather, an average J was used, where J$_{avg}$ = (^{1}J$_{CH}$ + ^{1}J$_{NH}$)/2, leading to an approximate 6% loss in sensitivity for both ^{1}H$_C$ and ^{1}H$_N$ resonances. In this report, an improved simultaneous

---

*To whom correspondence should be addressed.

^{13}C/^{15}N selection is presented, which compensates for the different magnitudes of $^{1}J_{CH}$ and $^{1}J_{NH}$ and also accommodates different ^{13}C and ^{15}N spectral widths in the simultaneous dimension. Boelens and co-workers have recently reported a similar approach, applied in a series of 2D heteronuclear correlation experiments (Boelens et al., 1994). Kay and co-workers have also recently published a non-sensitivity-enhanced 3D NOESY experiment, simultaneously edited in both ^{15}N and ^{13}C (Pascal et al., 1994). We have incorporated this approach into a gradient-enhanced *and* sensitivity-enhanced 4D NOESY experiment, to permit the simultaneous acquisition of a [^{13}C,^{15}N]/[^{15}N,^{15}N]-separated data set. Experimental results are presented for the 74-residue [^{13}C,^{15}N]-labeled N-terminal SH3 domain of mGrb2 (Suen et al., 1993), complexed with a peptide fragment from mSOS-2 (Bowtell et al., 1992) in 90% H$_2$O. A detailed analysis of artifacts is also presented in light of both the limited phase cycling generally available to 4D experiments and the high dynamic-range character of NOESY spectra relative to one-bond heteronuclear correlation spectra.

THEORY

Figure 1 presents two pulse sequences for performing the 4D gradient-enhanced, sensitivity-
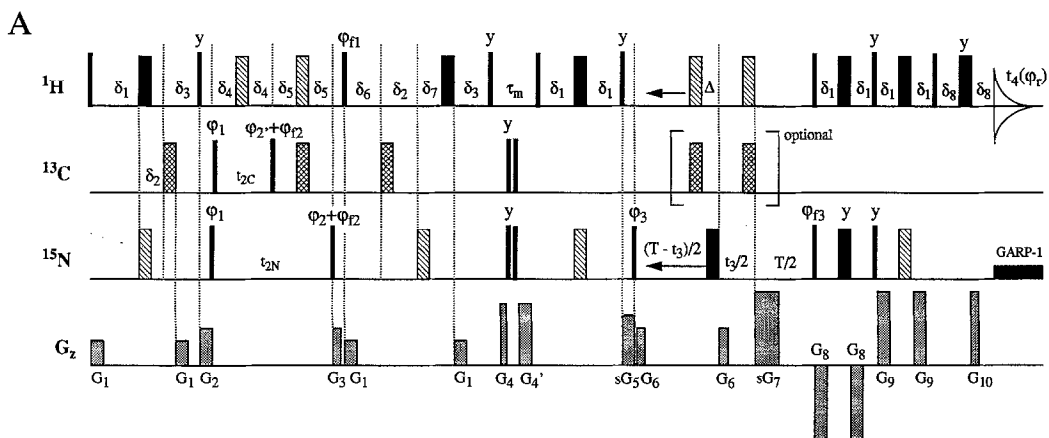

Fig. 1. The 4D gradient-enhanced, sensitivity-enhanced, and simultaneous [^{13}C,^{15}N]/[^{15}N,^{15}N]-NOESY pulse sequences: (A) constant-time t_3 evolution period; and (B) incremented t_3 evolution period. 90° pulses are represented by wide lines, simple 180° pulses by black rectangles, 90$_x$240$_y$90$_x$ composite inversion pulses (Levitt, 1986) by diagonally striped rectangles, and 90$_x$180$_y$90$_x$ composite inversion pulses by checkered rectangles (Levitt, 1986). Unless otherwise indicated, all pulses have phase x. For the optional ^{13}C decoupling pulses during t_3, the ^{13}C carrier was set midway between the ^{13}CO and ^{13}C$_\alpha$ spectral regions (~ 116 ppm). At all other times, the ^{13}C carrier was set at ~ 42 ppm. Complex data were collected in t_1 and t_2 (States et al., 1982) and in t_3 (Palmer II et al., 1991), with FIDs for φ_{f1} = (x,y), φ_{f2} = (x,y), and (φ_{f3} = (x,−x); s = (+1,−1) for G$_7$) being stored separately. States-TPPI (Marion et al., 1989) was employed on φ_{f1}, φ_1 and φ_3 for the t_1, t_2 and t_3 dimensions, respectively. For (^{15}N + ^{13}C) signals, $\varphi_{2'}$ = φ_2 + π; for (^{15}N − ^{13}C) signals, $\varphi_{2'}$ = φ_2. The FIDs for $\varphi_{2'}$ = φ_2 + π and $\varphi_{2'}$ = φ_2 were stored separately. 16 FIDs were therefore collected for each (t_1, t_2, t_3) time set. The phase cycle was φ_1 = φ_3 = x; φ_2 = x,−x; and φ_r = φ_2. The following acquisition parameters were used: t_{90}(^{1}H) = 6.1 μs, t_{90}(^{13}C) = 14.2 μs, t_{90}(^{15}N) = 46.6 μs, sw(F$_1$,^{1}H) = 8000 Hz, sw(F$_2$,^{13}C) = 4000 Hz, sw(F$_2$,^{15}N) = 1730 Hz, sw(F$_3$,^{15}N) = 1730 Hz, sw(F$_4$,^{1}H) = 11 000 Hz, t_4 = 69.81 ms, δ_1 = 2.50 ms, δ_2 = 0.71 ms, δ_3 = 1.79 ms, δ_4 = t_{2C}/2, δ_5 = (t_{2N} − t_{2C})/2, δ_6 = (t_1/2) + δ_3, δ_7 = t_1/2, δ_8 = 0.7 ms, T = 6.4 ms, τ_m = 80 ms, Δ = 0.2 ms (duration of G$_6$), and γB_2(^{15}N decouple) = 1.21 kHz with GARP-1 (Shaka et al., 1985). The t_2 evolution time was delayed by a half-dwell time, both to distinguish folded and unfolded ^{13}C resonances

enhanced, and simultaneous $[^{13}\text{C},^{15}\text{N}]/[^{15}\text{N},^{15}\text{N}]$-separated NOESY experiment, abbreviated as CN/NN-GESE-NOESY. In the following text, Fig. 1 refers to both Figs. 1A and B. There are two key features to the pulse sequences depicted in Fig. 1: (i) the ability to retain ^1H magnetization in t_1 that is directly coupled to either ^{13}C or ^{15}N in t_2; and (ii) the ability to accommodate different spectral widths for the $\text{C}^{\pm}\text{H}_z$ and $\text{N}^{\pm}\text{H}_z$ coherences during t_2. The sequence begins with a simultaneous INEPT transfer from ^1H to either ^{13}C or ^{15}N. Because $^1J_{\text{NH}}$ is significantly different from $^1J_{\text{CH}}$ in proteins, the initial INEPT transfer period must be simultaneously optimized for both $^1\text{H} \rightarrow {}^{13}\text{C}$ and $^1\text{H} \rightarrow {}^{15}\text{N}$ magnetization transfer, yielding

$$\delta_1 = \delta_{\text{NH}}/2 \tag{1a}$$

$$\delta_2 = (\delta_{\text{NH}} - \delta_{\text{CH}})/2 \tag{1b}$$

$$\delta_3 = \delta_{\text{CH}}/2 \tag{1c}$$

where $\delta_{\text{NH}} = 1/(2J_{\text{NH}})$ and $\delta_{\text{CH}} = 1/(2J_{\text{CH}})$. Equation 1 is predicated on $\delta_{\text{NH}} > \delta_{\text{CH}}$, a valid condition in proteins. The t_2 evolution time is designed to accommodate different spectral widths for the evolving $\text{C}^{\pm}\text{H}_z$ and $\text{N}^{\pm}\text{H}_z$ coherences. Figure 1 is depicted under the condition that
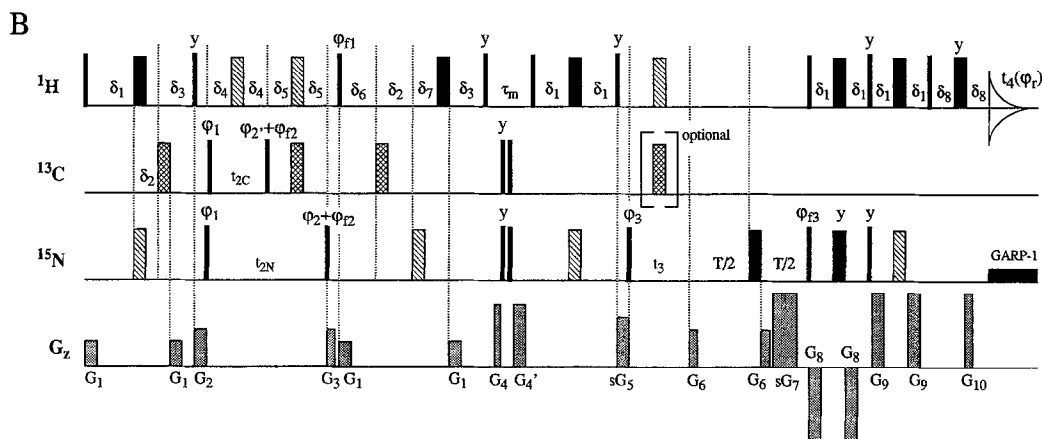
(Bax et al., 1991) and to eliminate baseline offset due to improper $t_2 = 0$ sampling. The t_3 evolution time was also delayed by a half-dwell time, to allow an additional pole to be used in the mirror-image linear prediction (Zhu and Bax, 1990) applied along this dimension. No ^{15}N resonances were folded in either F_2 or F_3. Sixty-four t_1, 18 t_2, and 10 t_3 increments were collected, yielding $t_1^{\text{max}} = 7.88$ ms, $t_{2C}^{\text{max}} = 4.38$ ms, $t_{2N}^{\text{max}} = 10.12$ ms and $t_3^{\text{max}} = 5.49$ ms. The following B_z gradient parameters were used: $G_1 = 2$ G/cm for 0.5 ms, $G_2 = 2$ G/cm for 1.2 ms, $G_3 = 2.3$ G/cm for 0.8 ms, $G_4 = 27$ G/cm for 2.7 ms, $G_{4'} = 27$ G/cm for 5.3 ms, $G_5 = 1$ G/cm for 1.0 ms, $G_6 = 8$ G/cm for 0.2 ms, $G_7 = \pm 32$ G/cm for 2.5 ms, $G_8 = -30$ G/cm for 0.3 ms, $G_9 = 30$ G/cm for 0.4 ms, and $G_{10} = 31.73$ G/cm for 0.25 ms. G_{10} was optimized relative to G_7 to yield the maximum ^1H coherence transfer echo. The total acquisition time was 138 h. The 4D data set was Fourier transformed to a final ReReReRe size of $128 \times 64 \times 64 \times 256$ $(F_1F_2F_3F_4)$, with digital resolutions of 0.10 ppm/point in F_1, 0.41 ppm/point in $F_2(^{13}\text{C})$, 0.45 ppm/point in $F_2(^{15}\text{N})$, 0.45 ppm/point in F_3 and 0.02 ppm/point in F_4. The t_3 dimension was the final one processed. Mirror-image linear prediction (Zhu and Bax, 1990) was used to extend the t_3 interferogram prior to Fourier transformation: 10 poles were used to extend t_3 by 16 complex points in the $[^{13}\text{C},^{15}\text{N}]$-separated spectrum and 8 poles to extend t_3 by nine complex points in the $[^{15}\text{N},^{15}\text{N}]$-separated spectrum. The 4D CN/NN-GESE-NOESY data set presented in Fig. 2 was collected at 30.0 °C on a Varian UnityPlus 600 spectrometer and processed on an SGI 4D/440VGX computer using an extensively modified version of FELIX 1.0 (Hare Research, Inc.).

$sw(^{13}C{:}t_2) > sw(^{15}N{:}t_2)$, but could easily be modified to handle $sw(^{13}C{:}t_2) < sw(^{15}N{:}t_2)$. The ^{13}C and ^{15}N t_2 evolution times, including a half-dwell delay, are calculated as

$$t'_{2N} = (n_{t2} - 0.5)/sw(^{15}N{:}t_2) - (4/\pi)\, t_{90}(^{15}N) - (28/3)\, t_{90}(^{1}H) - 6t_{90}(^{13}C) \qquad (2a)$$

$$t_{2N} = t'_{2N} + 6t_{90}(^{13}C) + (28/3)\, t_{90}\, (^{1}H) \qquad (2b)$$

$$t'_{2C} = (n_{t2} - 0.5)/sw(^{13}C{:}t_2) - (4/\pi)\, t_{90}(^{13}C) - (14/3)\, t_{90}(^{1}H) \qquad (2c)$$

$$t_{2C} = t'_{2C} + (14/3)\, t_{90}(^{1}H) \qquad (2d)$$

where n_{t2} is the t_2 increment number, $t_{90}(X)$ the length of the 90° pulse on nucleus X, and $1/sw(X{:}t_2)$ the dwell time for nucleus X in the t_2 dimension. t_{2C} and t_{2N} are the delays relevant to the pulse-sequence diagrams in Fig. 1; t'_{2C} and t'_{2N} are those relevant to the actual pulse-sequence program used to acquire the data. The multiplicative factors 28/3 and 14/3 for $t_{90}(^{1}H)$ in Eqs. 2a,b and 2c,d, respectively, arise due to the $90_x 240_y 90_x$ composite ^{1}H inversion pulses that are used during t_2 in Fig. 1 (Levitt, 1986). Equation 3 also insures that a first-order phasing constant of exactly 180° is required in F_2 (Marion and Bax, 1989). Using Eq. 2, the delays δ_4 and δ_5 can now be calculated as

$$\delta_4 = t'_{2C}/2 \qquad (3a)$$

$$\delta_5 = (t'_{2N} - t'_{2C})/2 \qquad (3b)$$

The reverse INEPT transfer from $^{13}C/^{15}N$ to ^{1}H, which follows the simultaneous $^{13}C/^{15}N$ t_2 evolution period, has strong similarities to the initial INEPT transfer. It differs, however, in the inclusion of a ^{1}H t_1 evolution time with simultaneous $^{13}C/^{15}N$ decoupling, using a minimal number of ^{13}C and ^{15}N composite inversion pulses. The total delay between the $90_{\varphi(f1)}(^{1}H)$ pulse and the $90_y(^{1}H)$ pulse immediately preceding the mixing time in Fig. 1 can be initially divided into four periods: δ_A, δ_B, δ_C, and δ_D. δ_A is the delay between $90_{\varphi(f1)}(^{1}H)$ and the ^{13}C composite inversion pulse; δ_B is the delay between the ^{13}C and ^{15}N composite inversion pulses; δ_C is the delay between the ^{15}N composite inversion pulse and the ^{1}H 180° refocusing pulse; and δ_D is the delay between the ^{1}H 180° refocusing pulse and the subsequent $90_y(^{1}H)$. From the experimental requirements, one can construct four simultaneous equations with these four delays:

$$\delta_A + \delta_B + \delta_C - \delta_D = t_1 \qquad (4a)$$

$$\delta_A - \delta_B - \delta_C + \delta_D = \delta_{CH} \qquad (4b)$$

$$\delta_A + \delta_B - \delta_C + \delta_D = \delta_{NH} \qquad (4c)$$

$$\delta_A + \delta_B + \delta_C + \delta_D = t_1 + \delta_{NH} \qquad (4d)$$

Equation 4a derives from ^{1}H chemical-shift considerations for a pure ^{1}H t_1 evolution time. Equations 4b and c are based on the optimization of $H^+C_z \rightarrow H^+$ and $H^+N_z \rightarrow H^+$ coherence rephasing by J_{CH} and J_{NH}, respectively. Finally, Eq. 4d is derived from the condition of minimum time. Under the assumption that $J_{NH} < J_{CH}$, the length of the total delay must be no greater than the sum of δ_{NH} and the ^{1}H evolution time t_1. Solving the set of simultaneous equations in Eq. 4, one obtains

$$\delta_A = (t_1 + \delta_{CH})/2 \qquad (5a)$$

$$\delta_B = (\delta_{NH} - \delta_{CH})/2 \qquad (5b)$$

$$\delta_C = t_1/2 \qquad (5c)$$

$$\delta_D = \delta_{NH}/2 \qquad (5d)$$

Comparing Eqs. 1 and 5, one observes that

$$\delta_B \equiv \delta_2 \qquad (6a)$$

$$\delta_D \equiv \delta_1 \qquad (6b)$$

The delays δ_A and δ_C are unique. Inspection of Fig. 1 reveals that δ_6 is equivalent to δ_A and δ_7 to δ_C. The delays defined by Eq. 5 allow one to achieve both a simultaneously optimized $H^{\pm}C_z \rightarrow H^{\pm}$ and $H^{\pm}N_z \rightarrow H^{\pm}$ coherence rephasing and $^{13}C/^{15}N$ decoupling in t_1, with only one ^{13}C and one ^{15}N composite inversion pulse.

$^{13}C/^{15}N$ editing

The simultaneous $^{13}C/^{15}N$ separation is practically achieved by collecting two FIDs, each with half the number of transients, for every FID normally collected in the standard 4D $[^{13}C,^{15}N]$-separated NOESY (Muhandiram et al., 1993). With reference to Fig. 1, $\varphi_{2'} = \varphi_2 + \pi$ for the first FID and $\varphi_{2'} = \varphi_2$ for the second FID, with which one collects $([^{15}N,^{15}N] + [^{13}C,^{15}N])$-separated and $([^{15}N,^{15}N] - [^{13}C,^{15}N])$-separated ^1H signals in t_4, respectively. The appropriate linear combination of these two FID sets during data processing readily allows one to construct either a pure 4D $[^{13}C,^{15}N]$-separated or a pure 4D $[^{15}N,^{15}N]$-separated NOESY spectrum.

$^{13}C/^{15}N$ cross-talk

A prerequisite for the success of the simultaneous $^{13}C/^{15}N$ separation is that no measurable interaction between the $(^1H,^{15}N)$ and the $(^1H,^{13}C)$ spin pairs occurs during the INEPT transfer period t_2, and/or the reverse INEPT transfer period; or that any coherence transfer pathway arising from such an interaction during these three periods be suppressed. The most serious artifact in the CN/NN-GESE-NOESY experiment is expected to arise from the $(^1H_C-^{13}C(t_2) \rightarrow {}^1H_N(t_1))$ magnetization transfer during the first half of the sequence. The ^1H_N magnetization at the end of t_1 gives rise to a cross peak in the $[^{13}C,^{15}N]$-separated NOESY spectrum with a $^1H(F_1)$ chemical shift that may be construed as arising from an aromatic ^1H. The amplitude of this cross peak, moreover, is proportional to the ^1H_N-^1H_N diagonal peak intensity in the $[^{15}N,^{15}N]$-separated NOESY spectrum and *may* therefore achieve an observable intensity in the $[^{13}C,^{15}N]$-separated spectrum. Other potential artifacts in the $[^{13}C,^{15}N]$-separated NOESY spectrum are expected to be proportional to a specific NOE intensity and are therefore less likely to be visible. In general, the dominant artifacts arising from $(^1H_C-^{13}C(t_2) \rightarrow {}^1H_N(t_1))$ magnetization transfer during the first half of the sequence will show up in the F_2-F_3 planes at $F_1 = F_4$ in the $[^{13}C,^{15}N]$-separated NOESY spectrum.

The most significant coherence transfer pathways that can lead to the stipulated $(^1H_C-^{13}C(t_2) \rightarrow {}^1H_N(t_1))$ magnetization transfer, and that do so *solely* by scalar coupling mechanisms,

will contain a $\sin^2$ dependence on only one weak scalar coupling. One such pathway involves the ^1H_N-$^{13}C_\alpha$ two-bond coupling. The phases of the ^1H pulses in the INEPT transfer mandate that the initial ^1H_N coherence couple to an odd number of spins or be suppressed by the $90_y(^1H)$-G_2 combination. One spin to which ^1H_N must actively couple is obviously $^{13}C_\alpha$. ^1H_N may also actively couple both to the amide nitrogen and to $^1H_\alpha$, resulting in a $(^1H_C$-$^{13}C(t_2) \to {}^1H_N(t_1))$ transfer pathway that contains a $\sin^2$ dependence on *two* weak scalar couplings, $^2J_{H(N)C\alpha}$ and $^3J_{HNH\alpha}$. The scalar transfer function for ^1H_N actively coupling only to $^{13}C_\alpha$ is

$$\sin^2 (\pi J_{H(N)C\alpha} \, \delta_{CH}) \cos^2 (\pi J_{HNH\alpha} \, \delta_{NH}) \cos^2 (\pi J_{H(N)N} \, \delta_{NH}) \tag{7}$$

and evaluates to a maximum of 0.009% for δ_{CH} = 3.57 ms, δ_{NH} = 5.56 ms, $J_{H(N)N}$ = 80–100 Hz, $J_{H(N)C\alpha}$ = 5.0 Hz, and $J_{HNH\alpha}$ = 9.0 Hz. The scalar transfer function for ^1H_N actively coupling to all three spins is

$$\sin^2 (\pi J_{H(N)C} \, \delta_{CH}) \sin^2 (\pi J_{HNH\alpha} \, \delta_{NH}) \sin^2 (\pi J_{H(N)N} \, \delta_{NH}) \tag{8}$$

and evaluates to a maximum of 0.008% under the same conditions. The ^1H_N-$^{13}C_\alpha$ two-bond coupling is therefore expected not to lead to a measurable artifact arising from $(^1H_C$-$^{13}C(t_2) \to {}^1H_N(t_1))$ magnetization transfer. If the initial ^1H coherence in the $(^1H_C$-$^{13}C(t_2) \to {}^1H_N(t_1))$ transfer pathway is on $^1H_\alpha$, then $^1H_\alpha \to {}^1H_N$ magnetization transfer must occur at some point for the coherence to end up on ^1H_N during t_1. Such a transfer during either the INEPT period or t_2 is rendered unobservable by the G_2 and G_3 pulsed-field gradients (PFGs). It also cannot occur during the reverse INEPT period, because there would have to be two 90° ^1H pulses after t_{2N} and prior to t_1 in order to bring about a COSY-type transfer from $^1H_\alpha$ to ^1H_N. Artifacts arising from ^{13}C-^{15}N scalar coupling during t_2 also require that $^1H_\alpha \to {}^1H_N$ magnetization transfer occur prior to t_1 and therefore meet with a similar fate.

Potential artifacts in the $[^{13}C,{}^{15}N]$-separated NOESY spectrum also arise from dipolar-mediated $(^1H_C$- $^{13}C(t_2) \to {}^1H_N(t_1))$ magnetization transfer. The intensity of these artifacts is proportional both to the intensity of the specific ^1H_C-^1H_N NOE cross peak and to $\sin(\pi J_{H(N)C} \, \delta_{CH})$, where $J_{H(N)C}$ is the scalar coupling constant between ^1H_N and the specific ^{13}C spin. The $J_{H(N)C}$ dependency limits the source and impact of these artifacts mainly to intraresidue $^1H_{\alpha/\beta}$-^1H_N NOE interactions. During the two δ_5 delays in Fig. 1, $C_{\alpha z}H_{\alpha z} \to C_{\alpha z}H_{NZ}$ magnetization transfer can occur by cross-relaxation. The 90° ^1H pulse at the end of the second δ_5 period effects $C_{\alpha z}H_{NZ} \to C_{\alpha z}H_N^\pm$. During the subsequent simultaneous $^{13}C/^{15}N$ reverse INEPT transfer, some of the $C_{\alpha z}H_N^\pm$ coherence can be refocused by the ^1H_N-$^{13}C_\alpha$ two-bond coupling. The scalar transfer function for the coherence refocusing is proportional to $\sin(\pi J_{H(N)C\alpha} \, \delta_{CH})$. If the NOE buildup remains linear at 80 ms (τ_m in Fig. 2), one can estimate that for δ_{CH} = 3.57 ms and $J_{H(N)C\alpha}$ = 5.0 Hz, the maximum intensity of this particular artifact is 0.4% of the normal intraresidue $^1H_\alpha$-^1H_N NOE intensity. If the NOE buildup has already become nonlinear at this τ_m value, then the preceding analysis underestimates the maximum intensity of this artifact. It is important to reiterate that essentially all of the aforedescribed artifacts align themselves *only* with intraresidue $^1H_\alpha$-^1H_N NOE cross peaks; normally resolved short-range and long-range interresidue NOE peaks are not distorted in this manner.

Gradients

All PFGs in this experiment are applied solely along the z-axis. The magnitude and duration of each PFG is listed in the legend to Fig. 1. Two pairs of PFGs, G_1, are applied during the first half of the sequence, both to eliminate artifacts (Bax and Pochapsky, 1992; Ruiz-Cabello et al., 1992) and to suppress radiation damping. It is imperative that the first PFG occur *immediately* after the initial ^1H 90° pulse. This prevents H_2O-induced radiation damping from attenuating any protein ^1H resonance whose chemical shift is sufficiently close to that of H_2O. In addition, each pair of G_1 PFGs serves to suppress artifacts arising both from incomplete ^1H excitation and refocusing and from incomplete $^{13}C/^{15}N$ inversion during both the INEPT and reverse INEPT transfer periods (Bax and Pochapsky, 1992; Ruiz-Cabello et al., 1992). The PFGs G_4 and G_4', separated by composite 90° pulses on ^{13}C and ^{15}N, are asymmetric in duration with a 1:2 ratio. The asymmetry attempts to minimize any gradient refocusing of undesired coherences. The PFG-RF pulse sandwich, $\{G_4$-$90_y(^{13}C/^{15}N)$-$90_x(^{13}C/^{15}N)$-G_4', eliminates single-quantum and heteronuclear zero-quantum coherences and attenuates homonuclear zero-quantum coherences by a factor of 2. Because there is no ^{15}N-^{15}N scalar coupling in the protein backbone, homonuclear zero-quantum coherences should not lead to detectable artifacts in this experiment. In the 4D $[^{13}C,^{13}C]$-separated NOESY experiment (Kay et al., 1990; Muhandiram et al., 1993), however, the complete elimination of ^{13}C-^{13}C zero-quantum coherences may become important. The PFG-RF sandwich is placed at the center of the mixing time τ_m, so that radiation damping has sufficient time to attenuate the amount of transverse H_2O magnetization for improved solvent suppression.

Because phase cycling is not superimposed on φ_3 to select ^{15}N single-quantum coherence in t_3, the G_5 and G_6 PFGs are extremely important in the suppression of artifacts in F_3. The G_2 and G_3 PFGs are correspondingly less important in suppressing artifacts in F_2, because φ_2 is cycled to select the $N^{\pm}H_{Nz} \rightarrow N_z/H_{Nz}$ coherence transfer pathway. For any residual or relaxation-induced N_zH_{Nz} J-ordered state in t_{2N}, the resulting $N_zH_{Nz} \rightarrow N^{\pm}H_{Nz}$ coherence transfer wrought by the $90_{\varphi2}(^{15}N)$ pulse is not suppressed by the φ_2 phase cycle and corresponds to one type of axial peak in F_2. This axial peak, moreover, is properly shifted to the edge of the F_2 spectrum by States-TPPI, superimposed on φ_1 (Marion et al., 1989). Because we have not folded the ^{15}N spectrum in F_2, artifacts on the edge of the F_2 spectrum are easily recognized. The G_3 PFG is therefore less important than G_6. In comparison to G_5, the requirements for G_2 are also reduced due to the absence of any ^{15}N 180° refocusing pulse during t_{2N}.

^{15}N coherence selection

^{15}N coherence selection in t_3 is achieved by a ^{15}N-^1H coherence transfer echo, brought about by the G_7 and G_{10} PFGs. Schemes for both a constant-time and an incremental t_3 evolution period are depicted in Figs. 1A and B, respectively. In a typical 4D experiment, the lower limit for the fixed delay T is a function of both the minimum duration of G_6 and G_7 and the minimum G_7-associated recovery time that yields a sufficiently high level of H_2O suppression. On our system, we have experimentally determined these times to be 0.2, ~ 2.5 and ~ 0.5 ms, respectively. The lower limit for T is therefore 6.4 ms. The use of PFGs for ^{15}N coherence selection avoids an additional two-step phase cycle on φ_3 and thereby preserves the minimum number of transients per FID at two. A sensitivity-enhanced ^{15}N-^1H reverse INEPT (Palmer II et al., 1991; Kay et al., 1992) is sandwiched between G_7 and G_{10} in Fig. 1. Both ^{15}N Cartesian components of the ^{15}N-^1H echo and anti-echo are detected simultaneously (Muhandiram and Kay, 1994), resulting in a

maximum sensitivity enhancement of two relative to the first published INEPT subsequences that both utilize a gradient-based coherence transfer echo and allow for a phase-sensitive presentation (Boyd et al., 1992).

The nature of the sensitivity enhancement requires that both the $\cos(\Omega_{H(N)}t_{evolve})$-modulated and the $\sin(\Omega_{H(N)}t_{evolve})$-modulated components of the resulting ^1H_N magnetization be simultaneously sampled. For the pulse sequences in Fig. 1, this requirement can only be met in the direct detection domain, t_4. The fact that only H_z magnetization can survive during τ_m forces the $90_y(^1H)$ pulse immediately preceding τ_m to select either the $\cos(\Omega_H t_2)$-modulated ($\varphi_{f1} = x$) or the $\sin(\Omega_H t_2)$-modulated ($\varphi_{f1} = y$) component of the ^1H single-quantum coherence – but *not both*! This method of sensitivity enhancement is therefore applicable to heteronuclear single-quantum coherences evolving in t_3 but not in t_2. The simultaneous selection of ^{13}C *and* ^{15}N coherences in a particular evolution period is most easily achieved by a concerted phase cycling of one ^{13}C and one ^{15}N rf pulse. The preceding two observations have therefore led us to select t_2 for the simultaneous $^{13}C/^{15}N$ evolution; and t_3 for ^{15}N coherence selection by gradient-based heteronuclear coherence transfer echoes.

G_7 and G_{10} are used both to select only acceptor ^1H spins that are attached to ^{15}N and, in conjunction with G_4, to achieve the majority of the per transient H_2O solvent suppression. G_7 is set to a magnitude of $\pm$ 32 G/cm, depending upon which complex t_3 components one is collecting, and has a duration of 2.5 ms. It is immediately followed by a recovery delay of 0.5 ms. The duration of G_{10} is set to 0.25 ms and its magnitude is adjusted to give the optimum ^1H signal in t_4. The sign of G_{10} is *always* positive because we have empirically observed that in our probe, recovery from positive PFGs occurs measurably faster than from negative ones. Under the aforementioned conditions, the magnitude of G_{10}, for which optimal coherence refocusing is achieved, has been determined to be $\sim$ 0.27 G/cm less than the corresponding magnitude of G_7 and furthermore, to be reasonably independent of the sign of G_7 (within 10 mG/cm). A phase-twist in the F_3 and F_4 lineshape can arise due to differences in the degree of coherence refocusing for the ^{15}N-^1H echo and anti-echo. By extending a previously published analysis (Eq. 22 in Muhandiram and Kay, 1994), one obtains for small differences in the absolute G_7^+ and G_7^- gradient strengths and short gradient times that the average relative signal intensity of the dispersive contribution, S_D, to the absorptive contribution, S_A, can be approximated by

$$< S_D/S_A > \sim -[2\pi \, h \, \lambda \, \gamma_N \, t_{G7} \, I_{G7+} \, (1 - \eta)]^2/12 \tag{9}$$

where 2h is the length of the ^1H rf coil in the NMR probe, λ the gradient efficiency of the PFG coil in G/cm/A, t_{G7} the duration of G_7, I_{G7+}, the amount of current used to generate G_7^+ and η the ratio of the achieved integrated current for a negative gradient pulse relative to a positive one for a duration t_{G7} at a fixed PFG amplifier setting. The additional B_z magnetic field due either to G_7^+ or G_7^- is assumed to be 0 at the center of the ^1H rf coil. γ_N is in units of Hz/G. Using h = 0.8 cm, λ = 3 G/cm/A, t_{G7} = 2.5 ms, I_{G7+} = 10.7 A and η = 0.9994, Eq. 9 evaluates to 0.09%. In this example, η = 0.9994 corresponds to a difference of 20 mG/cm between the G_7^+ (32 G/cm) and G_7^-(-31.98 G/cm) gradient magnitudes. A fivefold increase in this difference, however, yields $< S_D/S_A > \sim 2.4\%$. Test measurements on a concentrated sample of the $[^{13}C,^{15}N]$-Tyr-Asp dipeptide in d_6-DMSO have been conducted with a gradient-enhanced ^1H-^{15}N-HSQC sequence (Kay et al., 1992) in which the gradient applied to the ^{15}N single-quantum coherence has been progressively de-optimized. The

results demonstrate the onset of an F_3 and F_4 phase-twist for $\eta = 0.9969$ (data not shown), which corresponds to a difference of 100 mG/cm between the G_7^+ (32 G/cm) and G_7^- (−31.9 G/cm) gradient magnitudes. It is therefore important to minimize any such difference by adjusting G_{10} to achieve optimal coherence refocusing for both G_7^+ and G_7^- PFGs. In the data presented in Fig. 2, G_{10} was adjusted independently for G_7^+ and G_7^- to within 20 mG/cm of its optimum value. More-over, the difference between the two optimum values for G_{10} was no more than 10 mG/cm.

^{15}N constant-time evolution

The judicious use of PFGs around and during the constant-time t_3 evolution period in Fig. 1A is required to suppress several types of artifacts. States-TPPI is superimposed on φ_3 to shift F_3 axial peaks to the edge of that dimension (Marion et al., 1989). Consider the J-ordered state $H_{Nz}N_z$ immediately prior to the $90_{\varphi3}(^{15}N)$ pulse. A portion of the $H_{Nz}N_z$ state may either remain unexcited by the $90_{\varphi3}(^{15}N)$ pulse or be created by relaxation during the $(T - t_3)/2$ period. In either case, the action of an imperfect ^{15}N 180° pulse on an $H_{Nz}N_z$ state at the end of the $(T - t_3)/2$ period can give rise to an artifactual peak, whose F_3 chemical shift is given by

$$\Omega_{eff} = [\Omega(^{15}N) + sw(F_3)]/2 \tag{10}$$

These artifacts are referred to as type-1 artifacts. Type-1 artifacts are doublets in F_3, split by $J_{NH}/2$, and should present a distorted in-phase/antiphase lineshape due to $T_{min} > 0$. Only G_6 is involved in the suppression of type-1 artifacts. Note that T_{min} is the minimum duration of the constant-time period which can simultaneously accommodate both t_3^{max} and the G_6 and G_7 PFGs. Now consider the coherence $H_{Nz}N^{\pm}$ immediately prior to the $90_{\varphi3}(^{15}N)$ pulse. Such a coherence can be created by an imperfect ^{15}N 180° inversion pulse in the preceding INEPT transfer period. The $90_{\varphi3}(^{15}N)$ pulse can retain a portion of this coherence as $H_{Nz}N^{\pm}$, which can then give rise to an artifactual peak whose F_3 chemical shift is given by

$$\Omega_{eff} = \Omega(^{15}N) + [sw(F_3)/2] \tag{11}$$

These artifacts are referred to as type-2 artifacts. In contrast to the previous case, type-2 artifacts are singlets in F_3 and should present an in-phase lineshape. Only G_5 is involved in the suppression of type-2 artifacts. A symmetric pair of PFGs on either side of the $180(^1H)$-$180(^{15}N)$ pulse sandwich in this INEPT transfer period may provide additional suppression of type-2 artifacts. These two types of artifacts have been observed in the absence of G_5 and G_6 for the isotopically labeled Tyr-Asp dipeptide, using a 3D version of the 4D experiment with $t_1 = 0$ (data not shown). Improved values for these two PFGs were subsequently obtained using this test sample: $G_5 = 15$ G/cm for 0.8 ms and $G_6 = 15$ G/cm for 0.3 ms.

RESULTS

The pulse sequence in Fig. 1A was used to acquire the simultaneous 4D NOESY data set on the 74-residue isotopically labeled N-terminal SH3 domain of mGrb2 (Suen et al., 1993), complexed to a peptide fragment from mSOS-2 (Bowtell et al., 1992) in 90% H_2O. The protein concentration was 2.4 mM. The data were collected at 30.0 °C on a Varian UnityPlus 600 spectrometer. ^{13}C

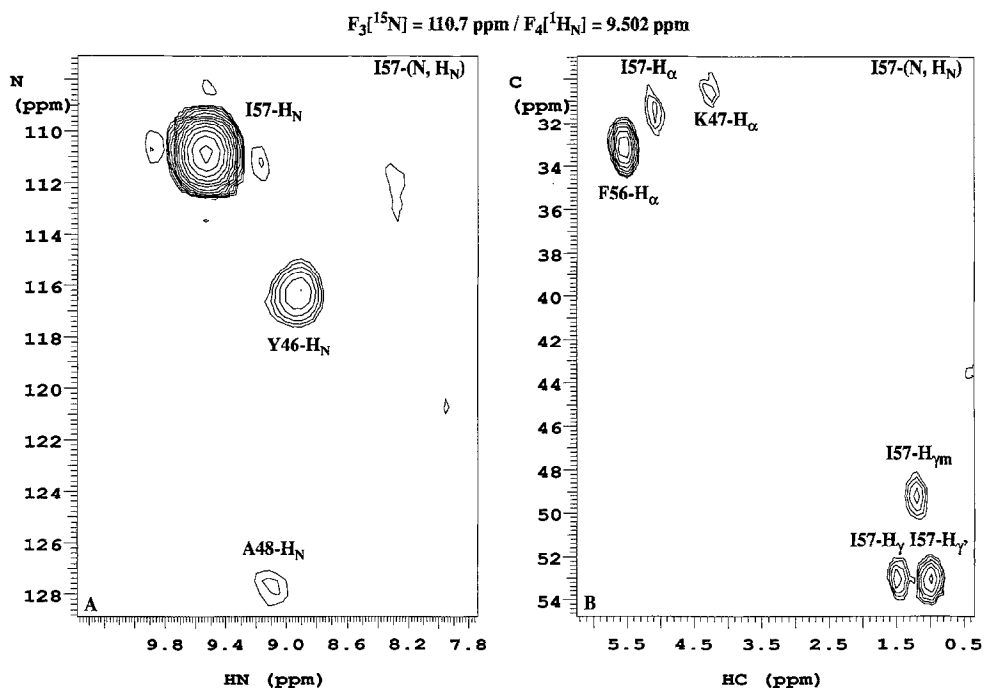$$F_3[^{15}N] = 110.7 \text{ ppm} / F_4[^1H_N] = 9.502 \text{ ppm}$$

Fig. 2. $F_1(^1H)F_2(^{15}N/^{13}C)$ donor planes locked on the acceptor ($^{15}N,^1H_N$) resonance frequencies of Ile[57]. (A) [$^{15}N,^{15}N$]-separated NOESY spectrum yielding ($^1H_N,^{15}N$) to ($^1H_N,^{15}N$) interactions. Cross-strand NOEs from both Tyr[46] and Ala[48] to Ile[57] are labeled. (B) [$^{13}C,^{15}N$]-separated NOESY spectrum yielding ($^1H_C,^{13}C$) to ($^1H_N,^{15}N$) interactions. Six NOEs to ($^{15}N, ^1H_N$) of Ile[57] are labeled: four intraresidue, one sequential from ($^1H_\alpha,^{13}C_\alpha$) of Phe[56] and one cross-strand from ($^1H_\alpha,^{13}C_\alpha$) of Lys[47]. These data were acquired with the pulse sequence in Fig. 1A, without ^{13}C decoupling pulses during t_3. For reference, residue M in our SH3 domain corresponds to residue M + 9 in the full mGrb2 protein (Suen et al., 1993).

decoupling pulses were not employed during t_3. For reference, residue M in our SH3 domain corresponds to residue M + 9 in the full mGrb2 protein (Suen et al., 1993). The $F_1(^1H)F_2(^{15}N/^{13}C)$ donor ($^1H_N,^{15}N$) and ($^1H_C,^{13}C$) planes, which are locked on the acceptor ($^{15}N,^1H_N$) resonance frequencies of Ile[57] in $F_3(^{15}N)F_4(^1H_N)$, are presented in Figs. 2A and B, respectively. In Fig. 2A, Tyr[46]-Ile[57] and Ala[48]-Ile[57] $^1H_N \rightarrow {}^1H_N$ cross-strand NOEs are evident. The ^1H_N diagonal peak for Ile[57] exhibits a clean lineshape, with minimal distortion at the base. Figure 3 presents a comparison of the F_3 and F_2 traces through the Ile[57]-H_N diagonal peak of Fig. 2A. The F_2 trace is remarkably clean. Both type-1 and type-2 artifacts, however, are evident in the F_3 trace (see Eqs. 10 and 11, respectively). The type-1 artifact is the largest, i.e., approximately 2% of the main peak. As mentioned previously, additional studies on an isotopically labeled model peptide have shown that increasing both G_5 from 1 G/cm for 1 ms to 15 G/cm for 0.8 ms and G_6 from 8 G/cm to 15 G/cm for the same duration (0.2 ms) *dramatically* reduces the magnitude of these two types of artifacts (data not shown). The latter values for G_5 and G_6 are to be used in all future experiments with this pulse sequence (Fig. 1A).

Figure 3 illustrates that F_3 is the dimension in the [$^{15}N,^{15}N$]-separated NOESY spectrum most susceptible to artifacts arising from the large ^1H_N diagonal peaks. To insure that the two NOE correlations in Fig. 2A are not artifacts, F_3 and F_4 traces through both peaks have been examined.
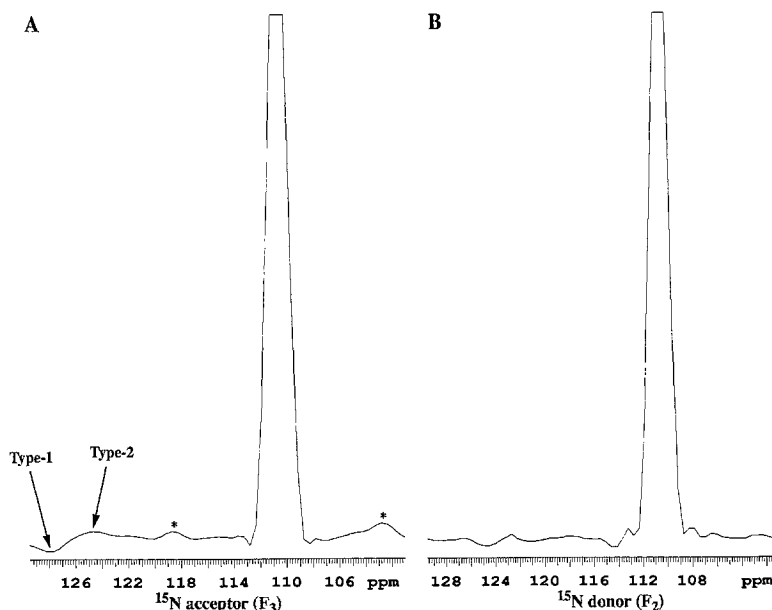
Fig. 3. A comparison of the (A) F_3 (^{15}N acceptor) and (B) F_2 (^{15}N donor) traces through the Ile^{57}-H_N diagonal peak in the [^{15}N,^{15}N]-separated NOESY spectrum of Fig. 2A. Both type-1 and type-2 artifacts in the F_3 trace (see the section on ^{15}N constant-time evolution) are indicated by arrows (Fig. 3A). The two artifacts indicated by * appear to be due to some long-term, periodic amplitude modulation in t_3. Note that t_3 is the dimension which is incremented the slowest. Compared to the F_3 trace, the corresponding F_2 trace (Fig. 3B) contains less artifacts.

In both cases, the NOE peak is the dominant one and therefore not an artifact arising from a large diagonal peak. In Fig. 2B, one cross-strand, one sequential and four intraresidue $^1H_C \rightarrow {}^1H_N$ NOEs are evident for Ile^{57}. Because there are no diagonal peaks in the 4D [^{13}C,^{15}N]-separated NOESY, Fig. 2B should be mostly free of artifacts.

Figure 4 shows the typical level of H_2O suppression achieved per FID throughout the course of the 4D experiment. It is important to note, however, that the level of H_2O suppression per transient is considerably worse. G_7 and G_{10} are the two critical gradients for H_2O suppression. To determine values for these two PFGs, our approach has been to set their magnitudes at the maximum value ($\sim$ 32 G/cm for our system) and then to decrease their duration to the point where a receiver overflow occurs at the maximum receiver gain. Provided that the final duration of G_7 is sufficiently short (2.5 ms in our case) relative to T_{2N}, this approach should yield the maximum achievable dynamic range for the protein ^1H resonances.

DISCUSSION

A key feature in the CN/NN-GESE-NOESY experiment is the ability to edit the 4D time-domain data in t_2 so that only one type of NOE interaction is presented: either $^1H_C \rightarrow {}^1H_N$ (CN) or $^1H_N \rightarrow {}^1H_N$ (NN). This editing ability dictates that the size of the 4D time-domain data set be twice as large for a given overall resolution, because twice as many FIDs must now be stored separately for each (t_1, t_2, t_3) data point. Since the minimum number of transients per FID is two,
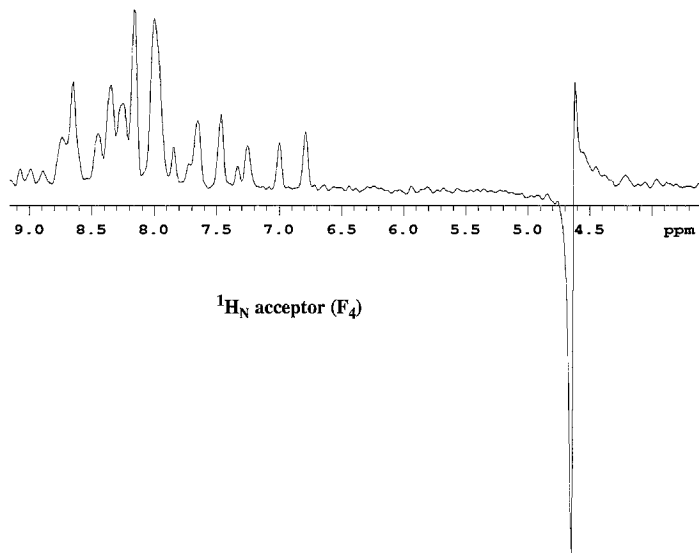
^1H_N acceptor (F$_4$)

Fig. 4. The first increment from the 4D CN/NN-GESE-NOESY data set, processed to yield $^1H_N \rightarrow {}^1H_N$ correlations. The level of H_2O suppression is typical of that obtained throughout the course of the experiment. No selective H_2O presaturation was used at any time during the experiment; only two transients were collected per FID.

the number of increments in one or more indirect dimensions must be decreased accordingly for a given total acquisition time. Typically, the number of t_1 (donor ^1H) and t_3 (acceptor ^{15}N) increments are decreased, thereby compromising resolution in these two dimensions. If one did not require the $^{13}C/^{15}N$ editing capability in t_2, the minimum number of transients per FID could be increased to four, thereby allowing one to cycle $\varphi_3 = (x,-x)$ for more robust artifact suppression in F_3. One might, however, choose to maintain two transients per FID and to increase the number of increments in one or more indirect dimensions accordingly. It is important to point out that per unit acquisition time, there is *no loss* in S/N associated with the $^{13}C/^{15}N$ editing in t_2. Finally, no artifacts due to $^{13}C/^{15}N$ cross-talk were observed.

The simultaneous acquisition of ^1H_C and ^1H_N NOE donor spins incurs some loss in sensitivity for the ^1H_C spins, due to the extended INEPT and reverse INEPT periods. For a 25 kDa protein, this loss can be estimated at no more than 20%. Consider $T_2(^1H_C) \sim 15$ ms and $T_2(^1H_N) \sim 20$ ms, which is representative of this protein size. With $J_{CH} = 140$ Hz and $J_{NH} = 90$ Hz and with these T_2 values, one obtains 4.94 and 3.23 ms for δ_{NH}^{opt} and δ_{CH}^{opt}, respectively (Farmer II et al., 1992). The magnetization transfer function during the INEPT and reverse INEPT periods can therefore be calculated for ^1H_C spins to be 0.64 if δ_{CH}^{opt} is used, or 0.52 if δ_{NH}^{opt} is used. This reflects a decrease in magnetization transfer of only 19%. One can minimize this sensitivity loss for ^1H_C even further by distributing some of the loss to the ^1H_N spins. For instance, if $(\delta_{NH}^{opt} + \delta_{CH}^{opt})/2$ is used for the INEPT and reverse INEPT delay times in the above example, the ^1H_C spins and ^1H_N spins experience only 9% and 6% decreases, respectively, relative to their maximum sensitivity. For the protein in this study, the decrease in sensitivity for the ^1H_C spins is estimated at only 10% under the conditions described in the legend to Fig. 1.

The number of increments chosen for each indirect dimension is determined by the desired resolution, the profile of <S/N> versus t^{max}, the method of data processing and the total acquisi-

tion time. Since the ^{15}N resonances are reasonably well resolved for this protein and more limited in number compared to ^{13}C resonances, resolution in t_3 is not at a premium. We have therefore chosen to minimize the number of increments in t_3, with 10–12 as a typical value, and to extend the data by mirror-image linear prediction (miLP; Zhu and Bax, 1990) prior to the Fourier transform. The t_3 dimension is ideally suited to miLP for the following reasons: (i) good ^1H_N dispersion; (ii) a limited number of ^{1}H-^{15}N correlations; (iii) no ^{15}N-^{15}N and small ^{13}C-^{15}N scalar couplings; (iv) a short t_3^{max} for good sensitivity; and (v) a truly stationary interferogram (with optional ^{13}C decoupling). The relatively short t_3^{max} also allows us to effectively neglect the small ^{13}C-^{15}N scalar couplings during t_3. For the data set presented in Fig. 2, the three ^{13}C-^{15}N couplings decrease the ^{15}N signal amplitude by only ~6% for $t_3 = t_3^{max}$. The presence of these couplings, moreover, does not abrogate the stationary nature of the t_3 interferogram. Inclusion of the optional ^{13}C decoupling pulses during t_3 would, however, eliminate this small source of ^{15}N amplitude modulation. Multiplication of the t_3 interferogram by $(\cos(\pi^1 J_{NC\alpha} t_3)\cos(\pi^1 J_{NCO} t_3))^{-1}$ would also largely remove the small effect of these ^{13}C-^{15}N couplings (Wittekind and Müller, 1993), without incurring the risk of any additional artifacts and/or excessive rf stress on the probe. Neither approach to remove the small ^{13}C-^{15}N scalar couplings has been applied to the data presented in Fig. 2.

For best results, we have applied linear prediction (LP) only in the last dimension processed, namely t_3. Two approaches can be used in extending the application of LP to additional dimensions. One can apply LP in the desired dimensions during the original course of processing. Low S/N and severe spectral overlap, especially in 4D NOESY experiments, generally limit this approach. The other approach is to perform either an inverse Fourier transform (IFT) on complex spectral data (Clore et al., 1990) or an inverse Hilbert transform (IHT) on real spectral data to regenerate the complex interferogram along a particular dimension after all dimensions have been subjected to an initial FT (Schussheim and Cowburn, 1987). Prior to LP, however, one must also multiply the regenerated interferogram by the inverse of the apodization function applied during the original course of processing. The S/N and the degree of spectral overlap are now optimal for LP in any dimension. Unfortunately, in our hands this approach has proven unreliable for increasing the resolution in F_2, often severely degrading the quality of the final spectral data. We have therefore chosen the t_1 and t_2 acquisition parameters so that LP need not be applied along those dimensions.

The number of increments in t_2 is generally limited to 16–20, a compromise between Fourier resolution and time-domain <S/N>. For ^{13}C, the F_2 < S/N> in a 4D experiment is largely determined by t_2^{max} and the number of homonuclear ^{13}C coupling partners. A ^{13}C spin can be coupled to at most three other ^{13}C spins, indicating that $t_2^{max} < 1/(6J_{CC}) \sim 4.5$ ms. Since a 4 kHz spectral width was used for $F_2(^{13}C)$ in Fig. 2B, the upper limit to the number of t_2 increments is approximately 19. At this point, the number of increments in the donor ^{1}H t_1 dimension is determined by the desired total acquisition time. Typically, 64–80 t_1 increments are collected.

As evidenced by Fig. 3, the t_3 evolution period in Fig. 1A is by far the most susceptible to artifacts, due in part to the CT nature thereof. The impact of type-1 artifacts, whose Ω_{eff} is described by Eq. 10, can be mitigated by replacing the CT t_3 evolution period (Fig. 1A) with an incremented period (Fig. 1B). In the latter case, States-TPPI correctly shifts type-1 artifacts to the edge of the spectrum in F_3, where they are much less likely to be construed as real NOE peaks. The importance of G_6 is therefore reduced in the latter case. The incremented t_3 evolution period

offers no advantages over CT with respect to type-2 artifacts. G_5 is therefore of critical importance for both pulse sequences depicted in Fig. 1. Both the constant-time and the incremented t_3 evolution periods yield approximately the same sensitivity for $t_3^{max} \le T_{min}$. For $t_3^{max} \gg T_{min}$, however, a higher sensitivity is achieved with the incremented t_3 evolution period.

It should be evident that an analogous experiment can be derived based on ^1H_C detection, the NC/CC-GE-NOESY experiment. For ^1H_C detection, we have observed that ^{13}C coherence selection by gradient-based heteronuclear coherence transfer echoes provides the best H_2O suppression and does not require the application of time-domain deconvolution during F_4 processing to minimize the residual H_2O signal (Farmer II et al., to be published). This obervation tends to be supported by the recent work of Kay and co-workers (Pascal et al., 1994). ^{13}C coherence echoes were not used in their experiment; the residual H_2O signal was minimized during F_3 processing by time-domain deconvolution. Due to the presence of extensive ^{13}C-^{13}C one-bond scalar couplings and of ^{13}C spins with more than one ^1H attached, however, the method of sensitivity enhancement used in Fig. 1 with gradient-based heteronuclear coherence transfer echoes cannot be used as successfully for an acceptor ^{13}C dimension in terms of both sensitivity (Schleucher et al., 1994) and the required level of H_2O suppression (Farmer II and Müller, unpublished observations). Relative to the *maximum* sensitivity enhancement achievable by this method for a CH ^1H resonance with no ^{13}C-^{13}C one-bond couplings, we estimate a 4% degradation for non-glycine H_α and 50% for glycine H_α resonances with selective CO decoupling during the first two δ_1 periods after t_3; 12% for other CH ^1H resonances; and 50% for CH_3 and other CH_2 ^1H resonances. If gradient-based heteronuclear coherence transfer echoes are instead used in the more conventional approach (Boyd et al., 1992), one should observe approximately the same sensitivity for glycine H_α and all CH_2 and CH_3 ^1H resonances compared to the sensitivity-enhanced method; 48% less for non-glycine H_α resonances; and 43% less for all other CH ^1H resonances. Therefore, if some form of gradient-based heteronuclear coherence transfer echo is used to select ^{13}C in the acceptor dimension (F_3), the sensitivity obtained in that $[^{15}N,^{13}C]$-separated NOESY will range from *at least* 4% to 50% lower than that obtained from the experiments depicted in Fig. 1.

Finally, $^1H_2(N) \rightarrow {}^1H_2(N)$ NOEs are not amenable to the method of sensitivity enhancement employed in Fig. 1. The extra ^1H-^{15}N coupling nulls the contribution from one Cartesian component of both the ^{15}N-^1H echo and anti-echo, in analogy to the degradation in performance already discussed for CH_2 ^1H resonances. Such NOEs are therefore attenuated by a factor of two relative to all other $^1H \rightarrow {}^1H_N$ NOEs. As indicated, $^1H_2(N) \rightarrow {}^1H_N$ NOEs are not affected in this manner.

CONCLUSIONS

We have demonstrated the simultaneous acquisition of a 4D gradient-enhanced and sensitivity-enhanced $[^{13}C,^{15}N]$- and $[^{15}N,^{15}N]$-separated NOESY. The method of implementation allows for different ^{13}C and ^{15}N spectral widths in t_2, but requires that the same number of increments be collected for the ^{13}C and ^{15}N t_2 interferograms. The two 4D spectra can be deconvolved during the processing stage by the appropriate linear combinations of separately stored FIDs. The interleaved nature of this simultaneous method could also lead to improved peak registration between the two 4D spectra. Finally, the $[^{13}C,^{15}N]$- and $[^{15}N,^{15}N]$-separated NOESY experiments are excellent candidates for simultaneous acquisition for the following reasons: (i) H_2O is required as

the solvent in both experiments; (ii) maximum sensitivity is achieved in the [^{13}C,^{15}N]-spectrum; (iii) ^{1}H$_N$ detection places lower demands on H$_2$O suppression; and (iv) ^{15}N should be more amenable than ^{13}C to resolution enhancement by linear prediction.

ACKNOWLEDGEMENTS

REFERENCES

Bax, A., Ikura, M., Kay, L.E. and Zhu, G. (1991) *J. Magn. Reson.*, **91**, 174–178.

Bax, A. and Pochapsky, S.S. (1992) *J. Magn. Reson.*, **99**, 638–643.

Boelens, R., Burgering, M., Fogh, R.H. and Kaptein, R. (1994) *J. Biomol. NMR*, **4**, 201–213.

Bowtell, D., Fu, P., Simon, M. and Senior, P. (1992) *Proc. Natl. Acad. Sci. USA*, **89**, 6511–6515.

Boyd, J., Soffe, N., John, B.K., Plant, D. and Hurd, R. (1992) *J. Magn. Reson.*, **98**, 660–664.

Clore, G.M., Kay, L.E., Bax, A. and Gronenborn, A.M. (1990) *Biochemistry*, **30**, 12–18.

Farmer II, B.T. (1991) *J. Magn. Reson.*, **93**, 635–641.

Farmer II, B.T., Venters, R.A., Spicer, L.D., Wittekind, M.G. and Müller, L. (1992) *J. Biomol. NMR*, **2**, 195–202.

Kay, L.E., Clore, G.M., Bax, A. and Gronenborn, A.M. (1990) *Science*, **252**, 411–414.

Kay, L.E., Keifer, P. and Saarinen, T. (1992) *J. Am. Chem. Soc.*, **114**, 10663–10665.

Levitt, M.H. (1986) *Prog. NMR Spectrosc.*, **18**, 61–122.

Marion, D. and Bax, A. (1989) *J. Magn. Reson.*, **83**, 205–211.

Marion, D., Ikura, M., Tschudin, R. and Bax, A. (1989) *J. Magn. Reson.*, **85**, 393–399.

Muhandiram, D.R., Xu, G.Y. and Kay, L.E. (1993) *J. Biomol. NMR*, **3**, 463–470.

Muhandiram, D.R. and Kay, L.E. (1994) *J. Magn. Reson. Ser. B*, **103**, 203–216.

Palmer II, A.G., Cavanagh, J., Wright, P.E. and Rance, M. (1991) *J. Magn. Reson.*, **93**, 151–170.

Pascal, S.M., Muhandiram, D.R., Yamazaki, T., Forman-Kay, J.D. and Kay, L.E. (1994) *J. Magn. Reson. Ser. B*, **103**, 197–201.

Ruiz-Cabello, J., Vuister, G.W., Moonen, C.T.W., Van Gelderen, P., Cohen, J. and Van Zijl, P.C.M. (1992) *J. Magn. Reson.*, **100**, 282–302.

Schleucher, J., Schwendinger, M., Sattler, M., Schmidt, P., Schedletzky, O., Glaser, S.J., Sørensen, O.W. and Griesinger, C. (1994) *J. Biomol. NMR*, **4**, 301–306.

Schussheim, A.E. and Cowburn, D. (1987) *J. Magn. Reson.*, **71**, 371–378.

Shaka, A.J., Parker, P. and Freeman, R. (1985) *J. Magn. Reson.*, **64**, 547–552.

States, D.J., Haberkorn, R.A. and Ruben, D.J. (1982) *J. Magn. Reson.*, **48**, 286–292.

Suen, K.-L., Bustelo, X.R., Pawson, T. and Barbacid, M. (1993) *Mol. Cell. Biol.*, **13**, 5500–5512.

Wittekind, M. and Müller, L. (1993) *J. Magn. Reson. Ser. B*, **101**, 201–205.

Zhu, G. and Bax, A. (1990) *J. Magn. Reson.*, **90**, 405–410.

Zuiderweg, E.R.P., Petros, A.M., Fesik, S.W. and Olejniczak, E.T. (1991) *J. Am. Chem. Soc.*, **113**, 370–372.